energies

MDPI

Article

Numerical Investigation of a Floating-Type Support Structure (Tri-Star Floater) for 9.5 MW Wind Turbine Generators

Kyeonguk Heo [1], Hongbae Park [2], Rae-Hyoung Yuck [3] and Daeyong Lee [2,*]

[1] Energy Innovation Research Center for Wind Turbine Support Structures, Kunsan National University, 558 Daehak-ro, Gunsan-si 54150, Republic of Korea
[2] Department of Wind Energy, The Graduate School, Kunsan National University, 558 Daehak-ro, Gunsan-si 54150, Republic of Korea; dcv003@naver.com
[3] Samsung Ship Model Basin, Samsung Heavy Industry, 217 Munji-ro, Yuseong-gu, Daejeon 34051, Republic of Korea
* Correspondence: daeyong.lee@kunsan.ac.kr; Tel.: +82-10-4490-0980

Abstract: A numerical investigation of floating-type substructures for wind turbine generators was conducted by using time-domain simulation. A Tri-Star floater for 8–10 MW generators, which was developed by Samsung Heavy Industries (SHI), was chosen as the floating substructure. To make the anchor system, catenary mooring lines, considering redundancy, were installed on the floater. The main sources of external force on the wind turbine generator are wind, waves, and currents. To consider severe environmental conditions, Design Load Cases (DLCs) 1.6 and 6.1 of the IEC guidelines (IEC 61400-3-1) were chosen. From the measured environmental data for the installation site, the main parameters for the simulation conditions were obtained. The tilt angle and horizontal movement of the floater and the mooring tension for the different mooring systems were checked. The response of the floater during the failure of the mooring was also studied, and the critical failure of the mooring was confirmed. During the failure of the mooring, the redundancy system worked well, in which the movement of the floater was constrained within the criteria for all scenarios.

Keywords: sea-keeping; mooring failure; support structure; floating offshore wind turbine (FOWT)

check for updates

Citation: Heo, K.; Park, H.; Yuck, R.-H.; Lee, D. Numerical Investigation of a Floating-Type Support Structure (Tri-Star Floater) for 9.5 MW Wind Turbine Generators. *Energies* **2023**, *16*, 7961. https://doi.org/10.3390/en16247961

Academic Editor: Eugen Rusu

Received: 31 October 2023
Revised: 23 November 2023
Accepted: 5 December 2023
Published: 8 December 2023

Copyright: © 2023 by the authors. Licensee MDPI, Basel, Switzerland. This article is an open access article distributed under the terms and conditions of the Creative Commons Attribution (CC BY) license (https://creativecommons.org/licenses/by/4.0/).

1. Introduction

Due to increasing environmental threats, decarbonization has become one of the biggest issues around the world. In the national plans for the power supply of each country, the continuous expansion of renewable energy has been confirmed. For instance, the European Union (EU) agreed that renewable energy would make up about 42.5% of the total power supply by 2030. In renewable energy, wind is one of the main resources because of its eco-friendly and sustainable properties. Since several decades ago, the use of wind energy has been researched and its capacity has grown continuously.

Wind turbines have mainly been installed in onshore regions in the past. However, this creates several problems, such as excessive noise and aesthetic issues, given that the size of wind turbines has become large. The installation sites of wind turbine generators have increasingly moved to offshore regions. Offshore wind turbines need additional structures beneath the wind tower, called the substructure, and additional grid lines for the transmission of electricity. Depending on the type of substructure, wind turbine generators can be classified into two types, i.e., fixed and floating. Most fixed substructures have similar geometry to fixed oil platforms, and representative examples are the jacket, monopile, and tripod types [1]. Although a total of 90% of offshore wind turbine generators have fixed substructures, several problems with wind turbine generators located near shore regions have appeared, and the most suitable installation sites have been occupied. Furthermore, it is known that the average wind speed becomes high and steady in deep sea areas, but the economic value of fixed substructures decreases as the water becomes

deeper. Consequently, floating substructures have increasingly been installed in regions with relatively deep water. They also have similar substructures to oil platforms such as spars, semi-submersible platforms, tension leg platforms (TLPs), etc. Until now, many studies and field installations have been conducted for spar-type substructures. One of them, Hywind Tampen, is the biggest offshore wind farm project, which has a total capacity of 88 MW, and a spar-type substructure has been used. Since a floating offshore wind turbine has additional costs for the anchor system, such as mooring lines and anchors, the LCOE (levelized cost of energy) of floating offshore wind turbines has been relatively larger than that of other wind turbine generators. To reduce LCOE, much research has been conducted. For instance, numerous floater shapes and materials have been developed, and the responses of several mooring systems have been researched continuously [2–4].

The analysis of floating wind turbines needs complex techniques that should consider both the wind and the marine conditions. The load and responses of wind turbines, towers, and substructures should be obtained instantaneously, for which the total solution needs a combination of results from various fields. It has been found that the so-called "aero-hydro-servo-elastic dynamics" should be considered in the analysis of floating offshore wind turbines [5–7]. Accordingly, several schemes for coupling the load and response induced by wind and waves have been developed [8]. Open-FAST is a representative tool for the analysis of floating offshore wind turbines, and it has been mainly used by research institutes and applied to various conditions [9]. The commercial software package Bladed has been commonly used for the analysis of onshore and fixed offshore wind turbines. Recently, Bladed enhanced its functions for floating substructures. For instance, ways to consider the hydrodynamic coefficients and quadratic transfer functions (QTFs) have been developed. Other commercial software such as Orcaflex and ANSYS AQWA R22, etc., which have been used for the design of offshore structures with mooring systems, have extended their functions for floating offshore wind turbines by enhancing the method of calculating the wind loads and coupling scheme of the wind turbine.

Not only the combination of all forces but each load on the structure should be considered properly for the design of floating offshore wind turbines. For the aerodynamic analysis of a wind turbine, many research institutes have used reference wind turbines (RWTs), which have been developed for the purpose of research. A representative 5 MW wind turbine provided by the National Renewable Energy Laboratory (NREL) has been used for a long time in research into offshore wind turbines [10]. Both fixed and floating wind turbine generators have been researched by using 5 MW NREL RWTs with various substructures. As the capacity of wind turbines has become increasingly large, the 10 MW wind turbine of the DTU (Danmarks Tekniske Universitet or the Technical University of Denmark) has been researched [11]. For instance, the Lifes50+ project systemically researched the dynamic response of two kinds of floater (OO-star semi and NAUTILUS-DTU10) with a DTU wind turbine by using the FAST model [12]. Recently, the International Energy Agency (IEA) developed a new model, and they have provided information for 15 MW wind turbines [13]. The UMaine VolturnUS-S reference platform for IEA wind turbines was also introduced, and several dynamic responses have been researched [14]. Hydrodynamic analysis should also be conducted for the design of substructures. In some cases, a similar process is needed for some offshore structures. For instance, the effect of linear and second-order hydrodynamic forces induced by irregular waves on a floater has been confirmed for anchor systems. In particular, a slowly varying force that could create low-frequency resonance in a mooring system has been researched [15,16]. There are also many other design points for substructures, such as the elastic response of the tower, mechanical vibrations, control systems, and so on. However, there has been no consensus about how to optimize both experiments and numerical simulations [17–19] because there are few data on the responses of floating wind turbines obtained from real sites.

In South Korea, huge projects for offshore wind farms have been planned, and several floaters for offshore wind turbines have been developed. One of them, the Tri-Star floater, which is a semi-submersible type of floater, was developed by Samsung Heavy Industries

(SHI) in 2021 for 8–10 MW wind turbines. In this study, a numerical investigation of several responses of the Tri-Star floater with the 9.5 MW VESTAS wind turbine was conducted by using a relatively simple method, which could be used for the initial design stage. The motion response of the floater and the mooring tension of different mooring systems were studied. The wind and current loads acted statically, and the maximum value of the responses was mainly focused on. In addition, the scenario of the mooring failing with a mooring redundancy system was assumed, and the corresponding results were checked. The rest of this paper is organized as follows. The formulation for the calculation of response is stated in Section 2. The numerical model of a 9.5 MW wind turbine generator and environmental conditions are introduced in Section 3. Numerical simulation and criteria are stated and discussion on the results is conducted in Section 4. The conclusion is drawn in Section 5.

2. Formulation

2.1. Coordinate System

Figure 1 shows a birds-eye view of a wind turbine generator. The X-coordinate has the same direction as the wind flow, and the Y-coordinate is in the cross-flow direction of the wind. The Z-coordinate is along the wind tower, which is vertical to the pontoon of the floater. The water's depth is 150 m.

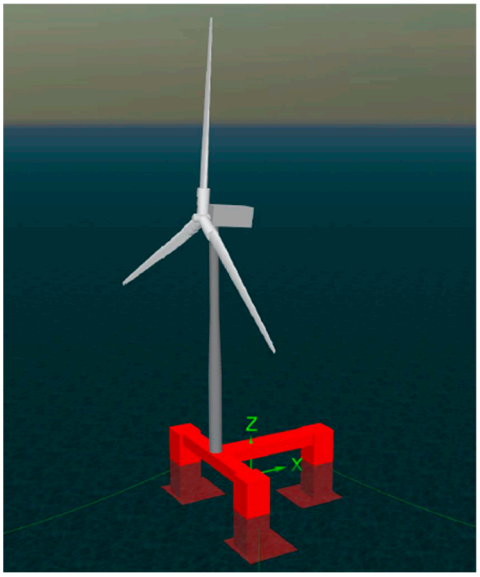


Figure 1. A wind turbine generator.

2.2. Equations of Motion

In regular waves, a linear time-harmonic is assumed, and the equation of motion is established in the frequency domain. It is written in the following form:

$$\sum_{j=1}^{6}\left\{-\omega^2\left(m_{jl}+a_{jl}\right)-i\omega\left(b_{jl}+b_{vis,jl}\right)+c_{jl}\right\}\xi_l = Af_j \tag{1}$$

where m_{jl} is the body mass matrix; a_{jl} and b_{jl} are the coefficients of added mass and wave radiation damping; $b_{vis,jl}$ is the viscous damping coefficient; c_{jl} is the hydrostatic stiffness matrix; A is the waves' amplitude; f_j is the waves' exciting force per unit of amplitude; and ξ_l is the response of complex motion. The subscripts j and l indicate the mode number of translational and rotational motions.

After solving the equation of motion, the response amplitude operator (RAO) of 6-DOF motions could be obtained in the frequency domain. Hydrodynamic coefficients and the corresponding RAO were calculated by using the commercial software ANSYS

R22. The calculation was based on the assumption of potential flow, and the other damping coefficients, such as viscous damping, were obtained from an experiment conducted by KRISO (Korea Research Institute of Ship and Ocean Engineering). Figures 2 and 3 show the response amplitude operator in the head and beam waves. It was confirmed that the heave and pitch in the head waves and the roll in the beam waves showed large reductions caused by the viscous effect near the resonance region.

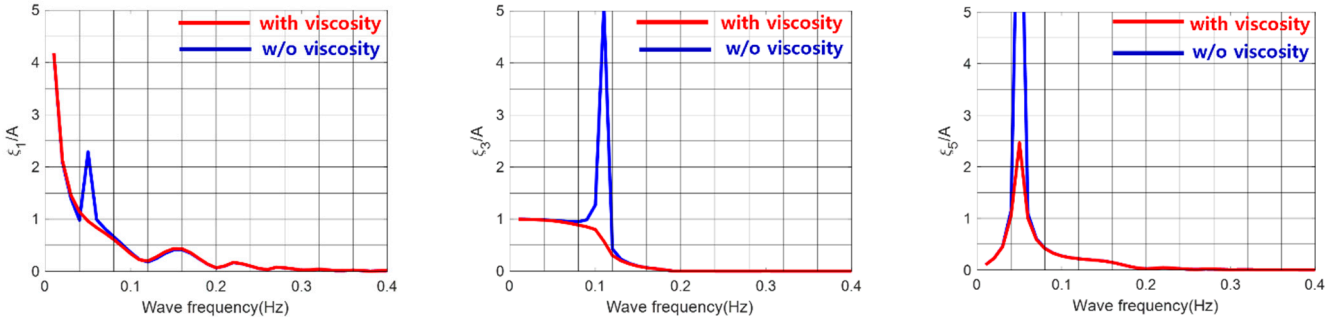


Figure 2. Response amplitude operator (RAO) of a Tri-Star floater in head waves (with and without the effect of viscosity).

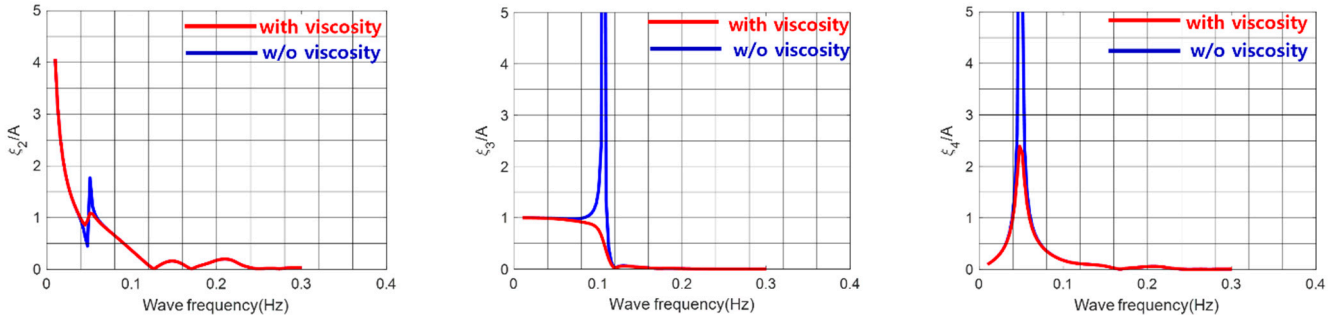


Figure 3. Response amplitude operator (RAO) of a Tri-Star floater in beam waves (with and without the effect of viscosity).

To obtain the motion responses in real sea conditions, time-domain computation was needed. Using the time-memory effect function (or retardation function), the equation of motion could be established in the time domain [20] as follows:

$$\sum_{j=1}^{6}\left\{\left(m_{jl}+a_{jl}(\infty)\right)\ddot{X}_l(t)+\int_{-\infty}^{t}L_{jl}(t-\tau)\ddot{X}_l(t)d\tau+c_{jl}X_l(t)\right\} = F^{(1)}_{wave,j}+F^{(2)}_{wave,j}+F_{mooring,j}+F_{current,j}+F_{wind,j} \tag{2}$$

where $a_{jl}(\infty)$ is the added mass at an infinite frequency, $X_l(t)$ is the instantaneous motion responses, $F_{wave,j}$ is the linear and second-order hydrodynamic forces, $F_{mooring,j}$ is the mooring's restoring force, $F_{current,j}$ is the current's force and $F_{wind,j}$ is the wind's force. The time-memory effect function can be expressed in the following form:

$$L_{jl}(t)=\frac{2}{\pi}\int_{0}^{\infty}\frac{1}{\omega}b_{jl}(\omega)\sin\omega t d\omega \tag{3}$$

It was assumed that a wind turbine generator receives several types of force from environmental conditions, and the forces of waves, currents, and winds were mainly considered. A mooring system was also installed on each column of the floater's anchor system. The methods of calculating each force are introduced in the following section.

2.3. Calculation of the External Forces

2.3.1. Wave Forces

Most commercial software for the problem of anchoring at sea adopts a weakly nonlinear assumption. In addition, a perturbation scheme that has a perturbation parameter proportional to the waves' slope (or amplitude) is applied. In line with these assumptions, the linear and second-order hydrodynamic forces are obtained via the following:

$$F_{wave,j}^{(1)} = \mathrm{Re}\left\{\sum_{n=1}^{N_w} A_n f_{jn}^{(1)} e^{-i(\omega_n t+\varepsilon_n)}\right\} \tag{4}$$

$$F_{wave,j}^{(2)} = \mathrm{Re}\left\{\sum_{n=1}^{N_w}\sum_{m=1}^{N_w} A_n A_m f_{jnm}^{-} e^{-i((\omega_n-\omega_m)t+\varepsilon_n-\varepsilon_m)} + \sum_{n=1}^{N_w}\sum_{m=1}^{N_w} A_n A_m f_{jnm}^{+} e^{-i((\omega_n+\omega_m)t+\varepsilon_n+\varepsilon_m)}\right\} \tag{5}$$

where N_w is the number of waves, and A_n is the amplitude of the nth wave. For the second-order forces, only the mean and a slowly varying component were considered in this analysis. In ANSYS, the quadratic transfer function (QTF) was calculated by using Newman's approximation [21], for which the quadratic transfer function is obtained from the time-averaged value of each frequency of the force, and there was no calculation of the second-order potential.

In the time-domain simulation, the waves' force could be calculated after obtaining the waves' amplitude for each frequency. The amplitude is generally extracted from the spectral density function of the waves' spectrum as follows:

$$A_n = \sqrt{2S(\omega_n)\Delta\omega} \tag{6}$$

For the irregular time-domain simulation, the JONSWAP spectrum [22] is used, and the spectral density function is as follows:

$$S(\omega) = \alpha^* H_s^2 \frac{\omega_p^4}{\omega^5} e^{-1.25\left(\frac{\omega_p}{\omega}\right)^4} \gamma^Y \tag{7}$$

$$where\ \ \alpha^* = \frac{0.0624}{0.230 + 0.0336\gamma - 0.185(1.9+\gamma)^{-1}} \quad on \quad 1 \le \gamma \le 7 \tag{8}$$

$$Y = e^{-\frac{\left(\frac{\omega}{\omega_p}-1\right)^2}{2\sigma^2}} \text{ and } \sigma = \begin{cases} 0.07 \ \ for \ \ \omega < \omega_p \\ 0.09 \ \ for \ \ \omega > \omega_p \end{cases} \tag{9}$$

where H_s is the significant wave height, ω_p is the peak frequency, and γ is sharpness of the waves' spectrum. In total, 100 waves were summed, and the phase of the wave force was chosen randomly. A scatter diagram of the significant wave height (Hs) and the peak period (Tp) was calculated from the data from NOAA (National Oceanic and Atmospheric Administration). In particular, the contour line of the significant wave height and the peak period was derived via the IFORM (inverse first-order reliability method) for environmental data [23]. The results of the 1-year and 50-year return periods for the significant wave height and the peak period are summarized in Table 1.

Table 1. Significant wave heights and peak periods of 1-year and 50-year return periods.

Return Period	H_s (Significant Wave Height, m)	T_p (Peak Period, s)
1 year	5.89	10.06 ± 1.5
50 years	8.14	11.50 ± 1.5

2.3.2. Mooring Restoring Forces

A floating body has no restoring force for horizontal translations and rotation of the vertical axis, i.e., surge, sway, and yaw motions. Thus, an anchor system should be installed on the floater. In general, the mooring system is attached to the floater as an anchor function. In this study, a chain catenary mooring system was used in the initial design stage. Calculation of the catenary mooring forces could be conducted in several ways, such as the dynamic, quasi-dynamic, and quasi-static methods. Among these, the quasi-static approach, which calculates the difference between the static mooring forces at each time step, was chosen for calculating the mooring's restoring forces.

From the equilibrium state of static force and the geometric relationships without considering the elasticity, the catenary equation for the static mooring line could be derived. Provided that the water becomes deeper, the long line of the catenary mooring will be influenced by the elastic effect. As described in [24], the relationship between mooring tension and the platform's position with elongation can be written in a closed form, as shown as follows and in Figure 4.

$$w(x - x_0) = \frac{T_{eH}^2}{EA}(\tan\varphi - \tan\varphi_0) + T_{eH}\left(\ln\frac{1+\sin\varphi}{\cos\varphi} - \ln\frac{1+\sin\varphi_0}{\cos\varphi_0}\right) \tag{10}$$

$$T_e \sin\varphi - T_{e0}\sin\varphi_0 = w(s - s_0) \rightarrow T_{eV} = T_{e0V} + w(s - s_0) \tag{11}$$

$$\widetilde{s} - \widetilde{s}_0 = s - s_0 + \frac{T_{e0H}}{2EA}\left\{\begin{array}{l}(s-s_0)\sqrt{1+\left(\frac{w(s-s_0)}{T_{e0H}} + \tan\varphi_0\right)^2} \\ + \frac{T_{e0V}}{w}\left(\sqrt{1+\left(\frac{w(s-s_0)}{T_{e0H}} + \tan\varphi_0\right)^2} - \frac{1}{\cos\varphi_0}\right) \\ + \frac{T_{e0H}}{w}\ln\left(\frac{\sin\varphi_0}{1+\sin\varphi_0} + \frac{1}{\sec\varphi_0+\tan\varphi_0}\left(\sqrt{1+\left(\frac{w(s-s_0)}{T_{e0H}} + \tan\varphi_0\right)^2} + \frac{w(s-s_0)}{T_{e0H}}\right)\right)\end{array}\right\} \tag{12}$$

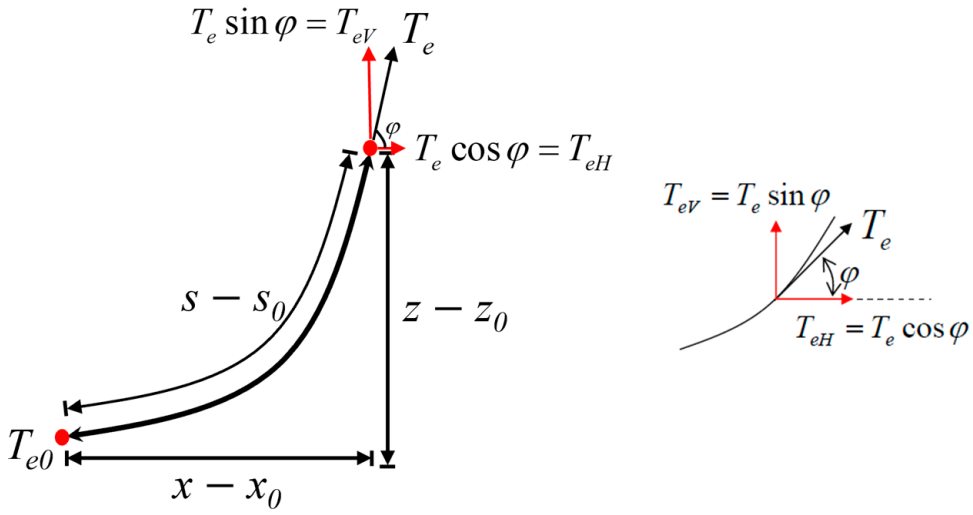


Figure 4. Definition of the variables in a catenary mooring system.

Here, T_e is the effective mooring tension; (x_0, z_0) and (x, z) are the positions in the x and z directions; w is the weight of each section; $(s - s_0)$ is the mooring line's length; (φ_0, φ) is the angle of the mooring at each position; and $(\widetilde{s} - \widetilde{s}_0)$ is the mooring line's length with elongation which comes from the elasticity of mooring line. In this study, elasticity was considered in the calculation of the static forces.

2.3.3. The Forces of the Current

It was assumed that the force of the current acts as a static force in the same direction as the waves. In this case, the current force is obtained in the same way as the calculation of drag force as follows:

$$F_{current,j} = \frac{1}{2}\rho_{water} C_D A_{projected} U_{current}^2 \quad (13)$$

where ρ_{water} is the density of seawater, C_D is the drag coefficient, and $A_{projected}$ is the projected area. Considering the shape of the floater, the drag coefficient for a square column with a corner radius was adopted. $U_{current}$ is the current's speed, which has been described in IEC 61400-3-1. As shown in the IEC guidelines, a current mainly consists of two parts. The first is the subsurface current generated by tides, storm surges, variations in atmospheric pressure, and so on. The other part is the wind-generated near-surface current. They are written in the following form:

$$U_{current}(z) = U_{ss}(z) + U_w(z) \quad (14)$$

$$U_{ss}(z) = U_{ss}(0)[(z+d)/d]^{1/7} \quad (15)$$

$$U_w(z) = U_w(0)(1 + z/60) \quad (16)$$

where U_{ss} is the subsurface current, and U_w is the near-surface current (Figure 5). The target installation site of a Tri-Star floater was the Donghae Gas Field (35.5 N, 130.0 E). For this site, the current's speed was obtained from Hybrid Coordinate Ocean Model (HYCOM) data. The current's speed at the water's surface and at −60 m is shown in Table 2 [25]. If we substitute the data in Table 2 into Equations (15) and (16), the current's speed at z = 0 can be obtained. After the current's speed profile has been obtained, the distributed force of the current is transformed into a point force which acts on the center of force (Figure 6).

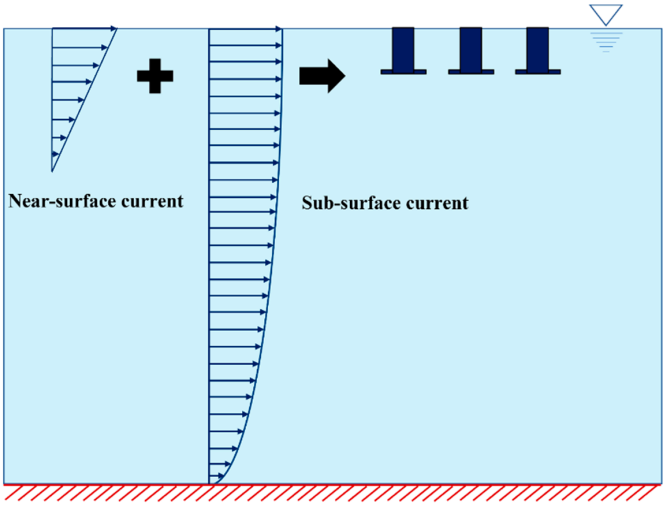


Figure 5. The current profile (near-surface and subsurface currents).

Table 2. Speed of the current for 1-year and 50-year return periods at z = 0 and −60 m (Choi and Kim, 2021).

Return Period	V_c (m/s) at 0 m	V_c (m/s) at −60 m
1 year	1.16	0.53
50 years	1.69	0.62

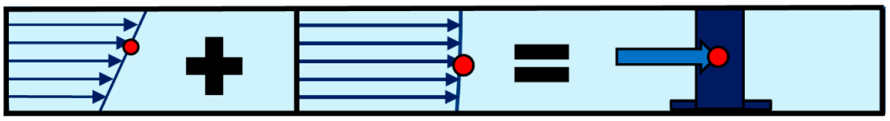


Figure 6. Transformation of the current's force.

2.3.4. Wind Forces

The wind force is calculated by the same method as the current force as follows:

$$F_{wind,j} = \frac{1}{2}\rho_{air} C_D A_{projected} U_{wind}^2 \quad (17)$$

where ρ_{air} is the density of air and U_{wind} is the wind speed. From the measured data for wind speed at several heights, as described in Table 3, the wind speed profile was approximated by using a power law as follows:

$$U_{wind}(Z) = U_{wind,Hub}(Z/Z_{Hub})^{0.11} \quad (18)$$

where Z_{Hub} is the hub's height and $U_{wind,Hub}$ is the wind speed at the hub. A comparison of the measured data and the results from Equation (18) is shown in Figure 7.

Table 3. Wind speed at each height.

Height (m)	1 Year (m/s)	50 Years (m/s)
10	23.67	31.92
20	25.33	34.41
50	27.52	37.69
100	29.19	40.17
128	29.78	41.06

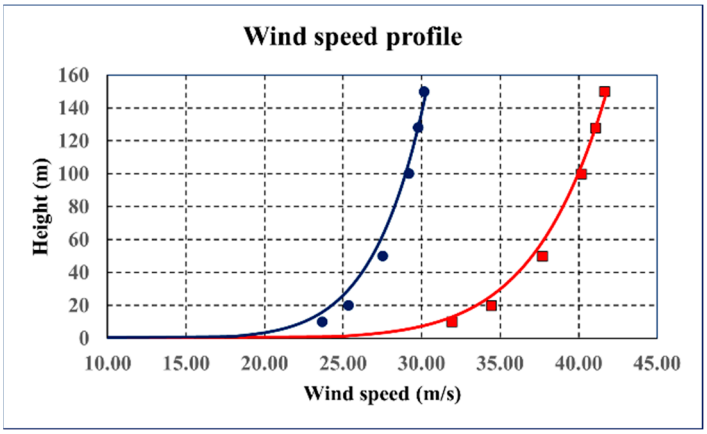


Figure 7. Comparison of the measured wind speed profile and that of the power law equation (points, measured data; line, approximated data; blue and red color are wind speed profile of 1-year and 50-year return periods).

As in the calculation of the force of the current, the wind force acts statically on the total structure. The distributed wind forces are transformed into point forces acting on the three main parts (the freeboard part of a floater, the wind tower, and the rotor blade), as shown in Figure 8. Among them, the wind force on the wind blade is obtained from the thrust curve of the blades for which the wind speed is lower than the cut-out wind speed (Figure 9).

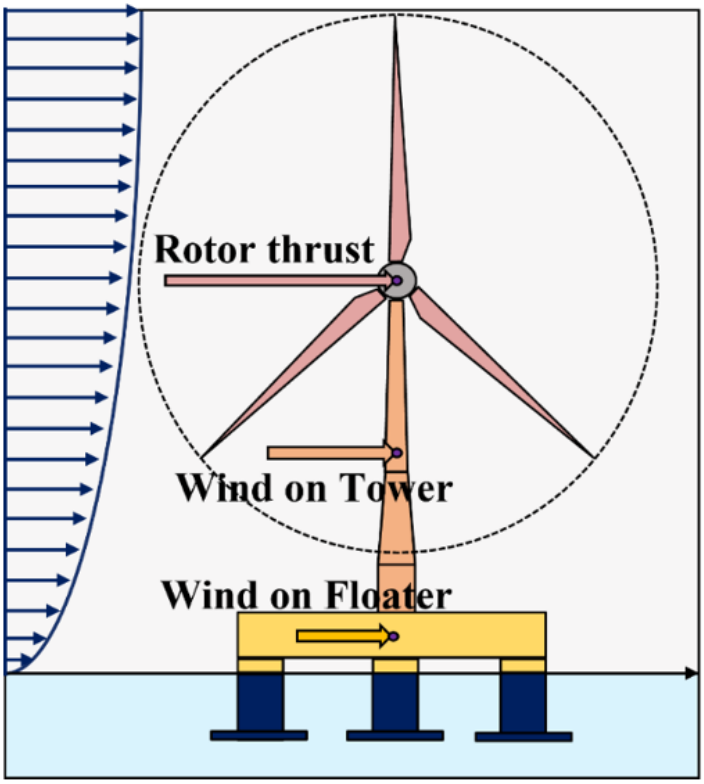


Figure 8. Area of wind force in a wind turbine generator.

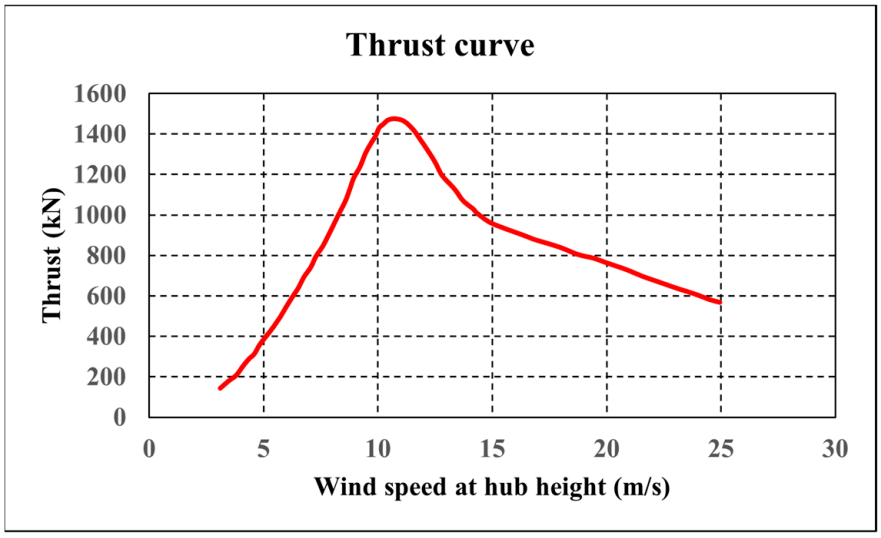


Figure 9. Thrust curve of the 9.5 MW VESTAS wind turbine.

3. Numerical Modeling

Generally, a floating offshore wind turbine constitutes a wind turbine, a wind tower, a floater, and a mooring system. The main dimensions of these for the simulation are introduced in this section.

3.1. Wind Turbine

In this study, a 9.5 MW VESTAS wind turbine was used. The dimensions of the wind turbine are summarized in Table 4.

Table 4. Principal dimensions of the wind turbine.

Parameter	Unit	Value
Output power	Megawatt	9.5
Rotor diameter	m	174.0
Hub diameter	m	4.0
Height of the hub from the bottom of tower	m	112.0
Nacelle mass	Megaton	295.0
Hub mass	Megaton	80.0
Blade mass	Megaton	105.0
Tower mass	Megaton	622.0
Rated wind speed	m/s	12.0
Rated rotor speed	rpm	9.9

3.2. Wind Tower

We chose the same shape of tower as used in the 3 MW wind turbine, which was installed in the southwest of the sea from Korea [26]. A wind tower generally has a cylindrical geometry, and its bottom part is thicker than the upper part to bear the structural loads. The main dimensions are shown in Figure 10. The overall size was scaled up from the 3 MW wind tower, which has been applied successfully in real sites, considering the height of the hub of the 9.5 MW wind turbine model.

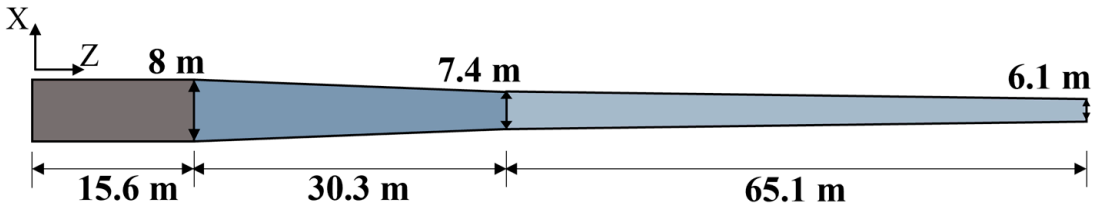


Figure 10. Main dimensions of the cylindrical wind tower.

3.3. Substructure

As introduced in previous chapters, the Tri-Star floater was used as the substructure of the wind turbine generator. This model was developed by Samsung Heavy Industries (SHI) for supporting 8–10 MW wind turbines. Their principal dimensions are shown in Table 5. It has three columns, which have a square section with a corner radius. At the top of the column, the pontoon is connected in a T-shape when viewed from the top. The bottom of the column has a square heave plate to increase the value of the hydrodynamic coefficient. To increase the stability, the floater has ballast water inside the columns. The center of mass of the total wind turbine system is located at the centroid of the triangle, for which each vertex is the center of the column.

3.4. Mooring System

For the numerical study, studless chain mooring lines were adopted, as summarized in Table 6. To consider the redundancy of the mooring lines, each fairlead point had two mooring lines. They were connected between the fairlead and the touchdown points. Figure 11 shows the floater with the mooring system used in this study. To investigate the effect of the mooring line's position, different touchdown points were selected, and two sets of touchdown points were finally determined after conducting a parametric study to confirm the effect of the suspended length. Each position of the mooring line is summarized in Tables 7 and 8.

Table 5. Dimensions of the Tri-Star floater.

Variable		Value
LOA (length overall) at draft level (m)		70.9
Breadth (m)		80
Column	Width (m)	12.0
	Height (m)	35.0
	Corner radius (m)	1.5
	Column-to-column distance (m)	68.0
Heave plate breadth (m)		25.0
Top pontoon	Max. length (m)	56.0
	Breadth (m)	10.0
	Height (m)	6.0
Displacement (megaton)		7863.3
Draft (m)		18.0
Total KG (bottom to CoG) (m)		27.26

Table 6. Principal dimensions of the R3 studless chain mooring.

Parameter	Unit	Value
Type	-	R3 studless
Length	m	900
Diameter	mm	153
Corrosion allowance	mm	8
MBL(uncorroded)	kN	16,579
MBL(incl. corrosion)	kN	14,483
Mass per unit of length	kg/m	465
Submerged weight	kg/m	407
Elastic modulus	kN/m^2	5.44×10^7

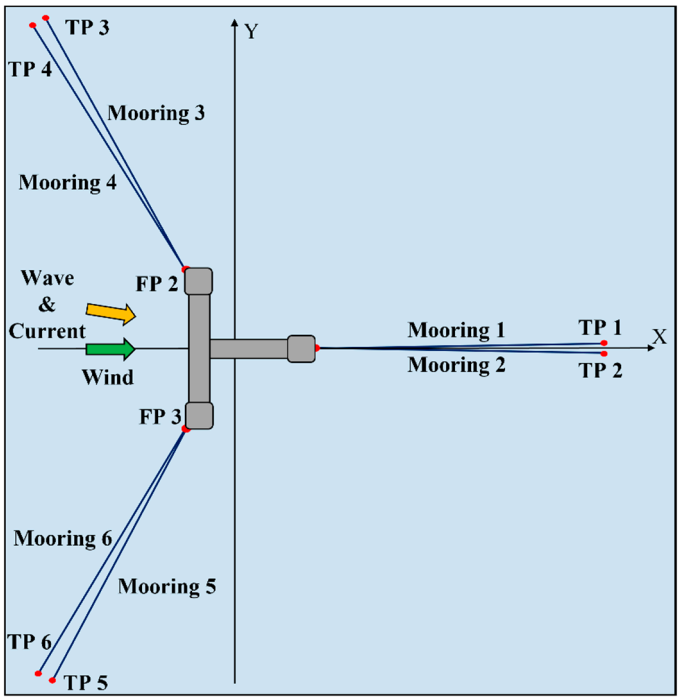


Figure 11. The floater with the mooring system. FP, fairlead points; TP, touchdown points (Yellow arrow means wave & current direction, Green arrow means wind direction).

Table 7. Coordinates of the fairlead points.

Points	Coordinates (X, Y, Z)
Fairlead point (FP) 1	(45.4, 0.0, 6.0)
Fairlead point (FP) 2	(−24.7, 39.1, 6.0)
Fairlead point (FP) 3	(−24.7, −39.1, 6.0)

Table 8. Coordinates of the touchdown points.

Points	Coordinates (X, Y, Z)	
	Horizontal Length: 840 m	Horizontal Length: 850 m
Touchdown point (TP) 1	(885.1, 22.0, −150.0)	(895.1, 22.3, −150.0)
Touchdown point (TP) 2	(885.1, −22.0, −150.0)	(895.1, −22.3, −150.0)
Touchdown point (TP) 3	(−425.6, 777.3, −150.0)	(−430.3, 786.1, −150.0)
Touchdown point (TP) 4	(−463.6, 755.3, −150.0)	(−468.9, 763.9, −150.0)
Touchdown point (TP) 5	(−425.6, −777.3, −150.0)	(−430.3, −786.1, −150.0)
Touchdown point (TP) 6	(−463.6, −755.3, −150.0)	(−468.9, −763.9, −150.0)

4. Numerical Simulation

4.1. Design Criteria for Floating Substructures

For the motion responses of a floating offshore wind turbine, there are three main design criteria (Figure 12) [27]. The first is the tilt angle of the floater. The maximum tilt angle should be lower than 10 degrees, and the mean value should also be lower than 5 degrees. The second is the horizontal acceleration at the RNA (rotor–nacelle assembly) of the floater. It is recommended that the acceleration in the direction of the wind at the RNA's position should be less than 0.3 g (gravitational acceleration), and that in the cross-flow direction should be less than 0.35 g in severe environmental conditions. A floater should keep its horizontal position within 40 m in relatively mild conditions, and it must have a maximum value of <60 m. In this study, the floater's tilt angle and horizontal movement were checked. The acceleration was also calculated, but we expected that it would have a relatively low value because the wind force simply acted statically in this study.

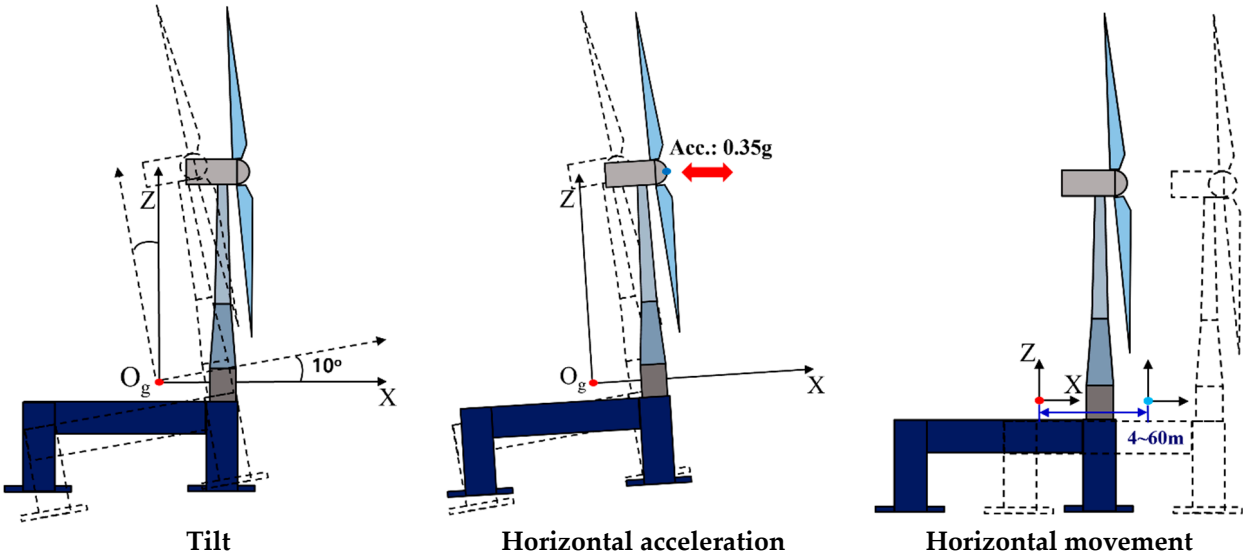


Figure 12. Criteria for floating substructures [27].

4.2. The Responses of a Floating Offshore Wind Turbine for Design Load Cases (DLCs)

To conduct a numerical investigation, the design load cases (DLCs) given in IEC 61400-3-1 were adopted. The severe environmental conditions in the design load cases (DLCs) of IEC 61400-3-1 were considered. Thus, DLCs 1.6 and 6.1 were chosen as the simulation

conditions in this study. In DLC 1.6, several environmental conditions, including a 1-year return period, were selected. To confirm the long-term conditions, two cases in DLC 6.1 were also chosen, and a 50-year return period was applied. The list of the environmental parameters of the simulated cases is described in Table 9. In all cases, the wind, waves, and current acted in a co-linear direction, except in Case 7, in which the waves and the current had a 15° angle of incidence.

Table 9. Design load cases (DLCs).

Cases	DLCs	Wind Speed (m/s)	H_s (m)	T_p (s)	Waves and Current—Wind Misalignment
1-1	1.6	9.6	4.97	8.04	0
1-2				9.59	0
1-3				11.14	0
2-1		11.0	5.12	8.16	0
2-2				9.74	0
2-3				11.31	0
3-1		13.0	5.55	8.49	0
3-2				10.14	0
3-3				11.78	0
4-1		20.0	6.57	9.24	0
4-2				11.03	0
4-3				12.82	0
5-1		25.0	7.28	9.73	0
5-2				11.61	0
5-3				13.49	0
6-1	6.1	41.09	8.12	10	0
6-2				11.5	0
6-3				13	0
7-1				10	15
7-2				11.5	15
7-3				13	15

In this study, a 5 h simulation was conducted, and the response after 1 h was checked to not include the transient initial responses. Figures 13 and 14 show the movement in the x-direction of the floater and the pitch angle in Case 2-1. In Case 2-1, the wind speed was 11 m/s, at which the rotor received the maximum thrust from wind force. In Figure 13, the blue and gray lines indicate the horizontal (x-direction) movement when the mooring lines had a horizontal length of 840 m and 850 m. It was confirmed that the floater had a small enough horizontal movement, which was lower than the maximum (40 m) for both lengths of the mooring line. Next, Figure 14 shows that the pitch angle was also small enough, as it was just below 5 degrees in the simulation. It was found that the pitch angle was not so sensitive to the suspended lengths. This is natural because the pitch motion already has some restoration from the hydrostatic force.

As well as the motion response of the floater, the tension of each mooring line under different environmental conditions was also confirmed. Figure 15 demonstrates the number of mooring lines and the main direction of mooring tension. In this study, the tension of Mooring Lines (1) and (3) was mostly checked in conditions of head waves.

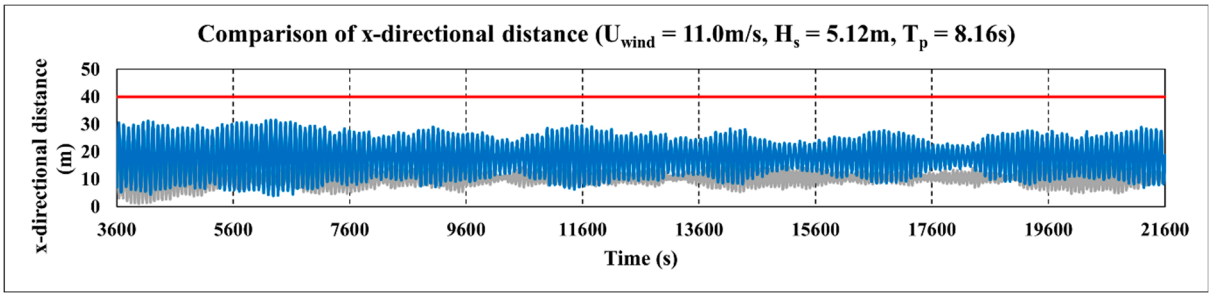


Figure 13. Comparison of movement in the x direction of a Tri-Star floater at different mooring positions (Case 2-1; blue, 840 m; gray, 850 m).

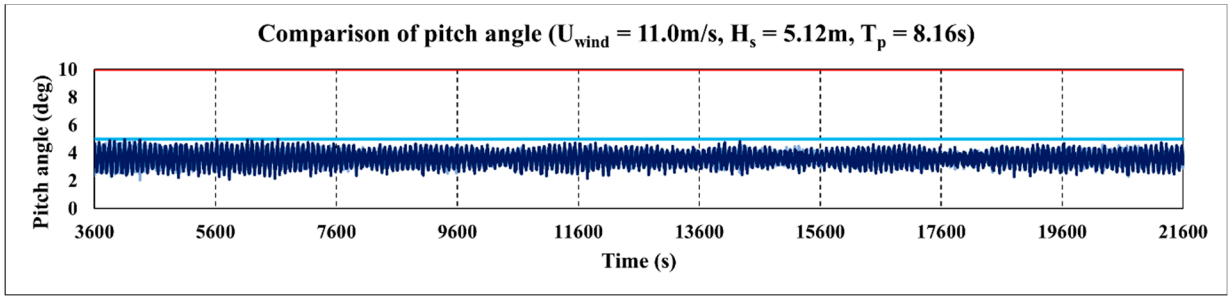


Figure 14. Comparison of the pitch angle of the Tri-Star floater at different mooring positions (Case 2-1).

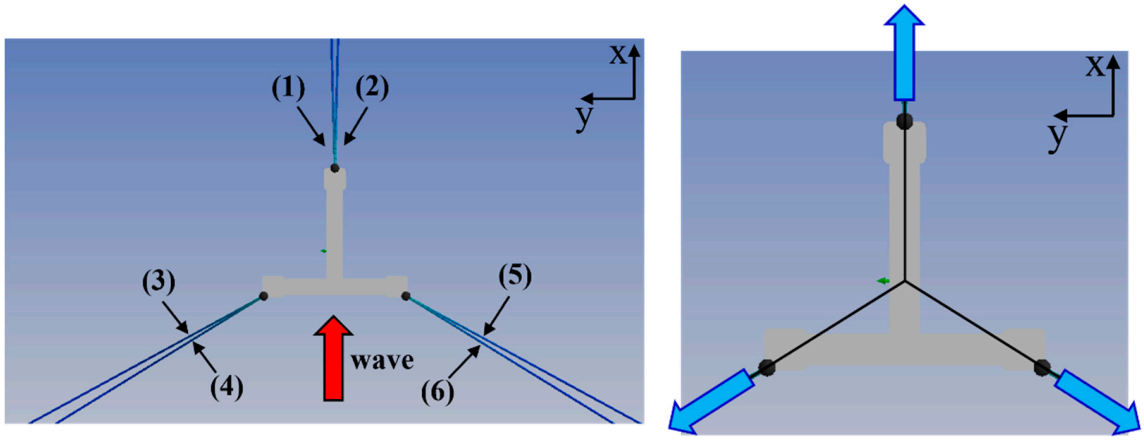


Figure 15. The number of mooring lines and the direction of mooring tension (Blue arrow).

Figure 16 demonstrates the tension of Mooring Lines (1) and (3). It shows that a small horizontal movement happened with longer mooring lines, and the mooring tension became larger because of the strong restoring forces. As deduced from Figure 15, the tension of Mooring Lines (1) and (2) was proportional to the negative surge motion, and that of other mooring lines increased when the floater had a positive surge motion.

Figures 17 and 18 show the responses for Case 6-1, in which a 50-year return period for the waves and current was applied. Since the wind speed was larger than the cut-out speed, the rotor's thrust suddenly decreased in this simulation. Due to the high significant wave height, the horizontal movement was relatively large, but it was smaller than 40 m for both lengths of the mooring line. In Figure 17, it is seen that the maximum pitch angle was very small. It can also be seen that the mean angle is much smaller than that in Case 2-1 because of the reduction in wind thrust. Finally, it can be seen that the mooring lines' tension is larger in Figure 19 due to an increase in horizontal movement, especially when the mooring lines are relatively long.

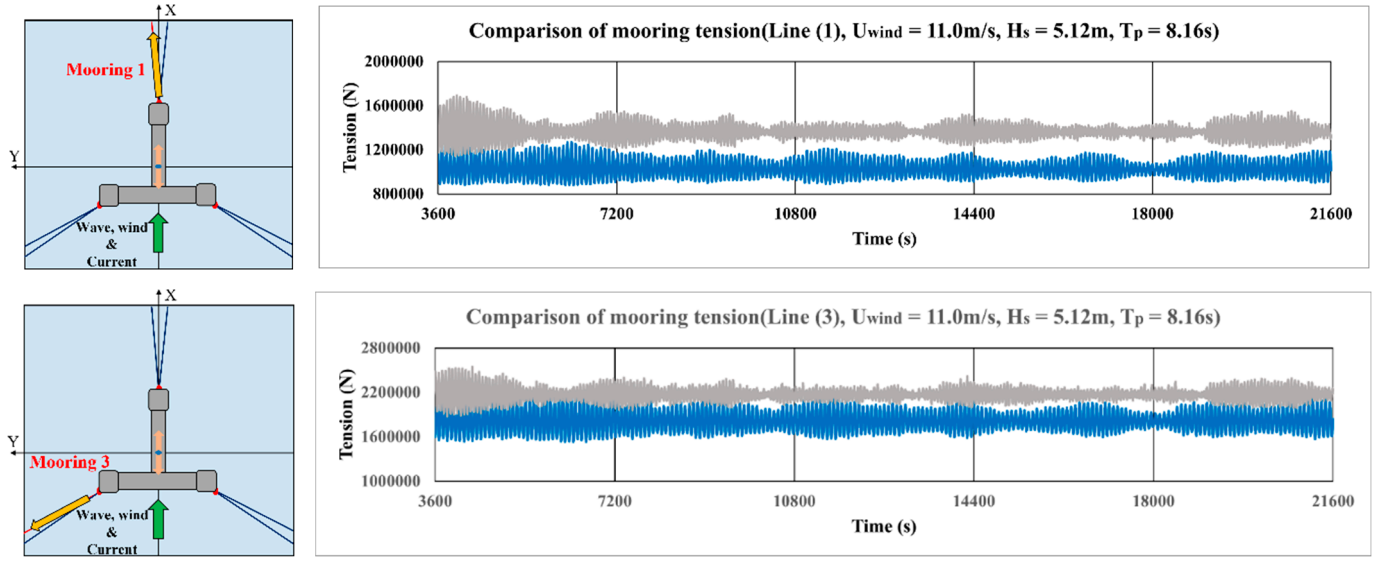


Figure 16. Comparison of mooring tension (Lines 1 and 3) at different mooring positions (Case 2-1; blue, 840 m; gray, 850 m; Yellow arrows mean direction of tension, Green arrow means direction of environmental loads).

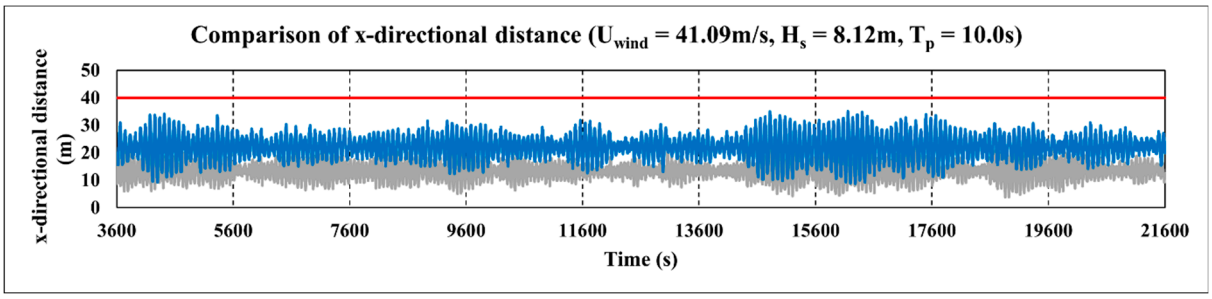


Figure 17. Comparison of movement in the x directional of a Tri-Star floater at different mooring positions (Case 6-1; blue, 840 m; gray, 850 m).

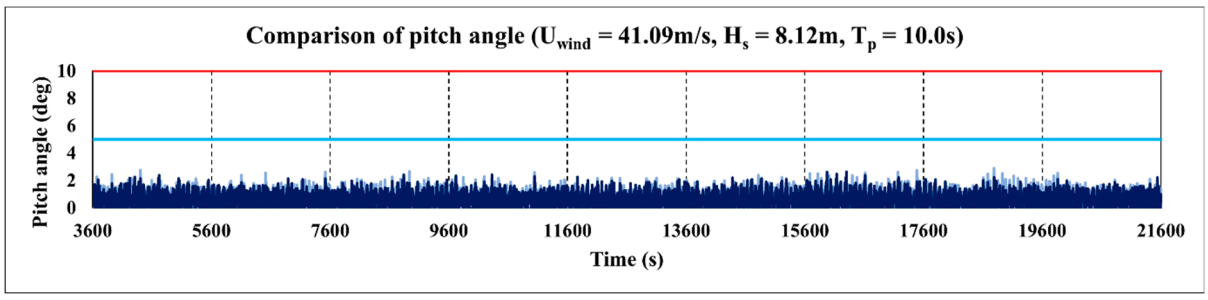


Figure 18. Comparison of the pitch angle of a Tri-Star floater at different mooring positions (Case 6-1).

The maximum and mean values of the motion responses in the simulations of all cases described in Table 8 are summarized in Figures 20 and 21. It was confirmed that the horizontal movement was generally large for DLC 6.1 (Cases 6-1–3, Cases 7-1–3). On the other hand, the tilt angle of the floater was relatively large for DLC 1.6 because of the huge wind thrust at the wind turbine. In particular, the mean value of the pitch angle decreased substantially in DLC 6.1. The maximum and mean tension of Mooring Lines 1 and 3 are summarized in Figures 22 and 23. Under head wave conditions, the maximum value of mooring tension was different in each case, but the mean value was generally similar in all cases.

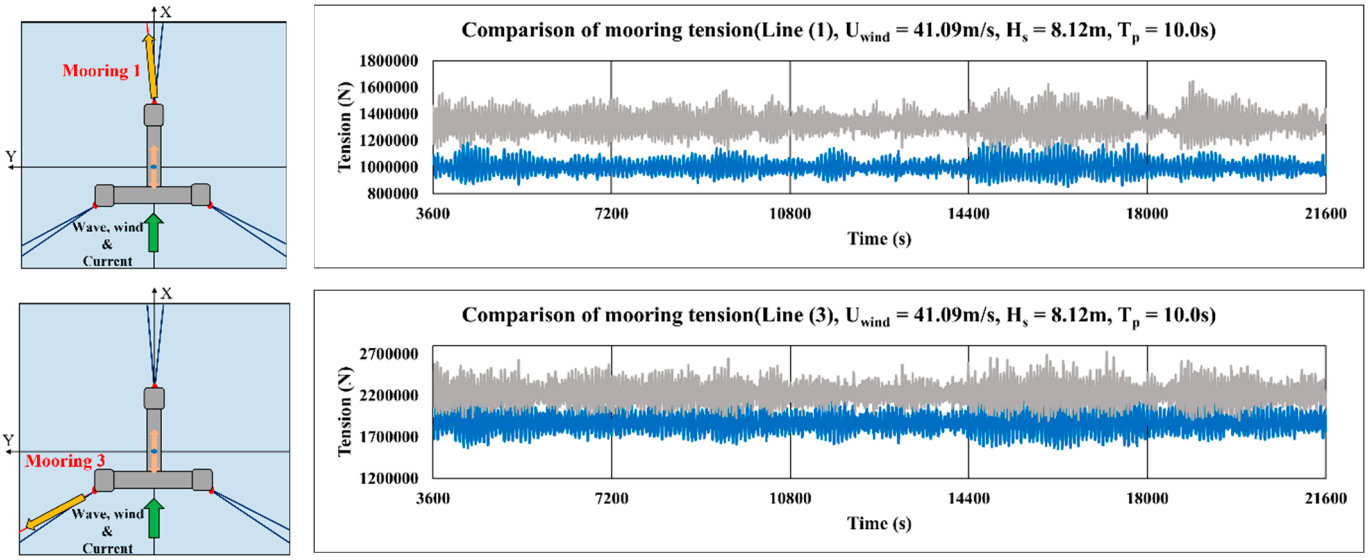


Figure 19. Comparison of mooring tension (Lines 1 and 3) at different mooring positions (Case 6-1; blue, 840 m; gray, 850 m; Yellow arrows mean direction of tension, Green arrow means direction of environmental loads).

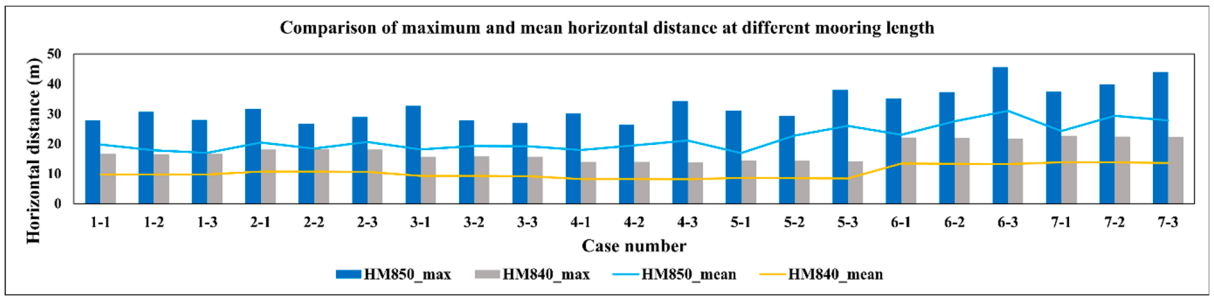


Figure 20. Comparison of the maximum and mean value of horizontal movement at different mooring positions.

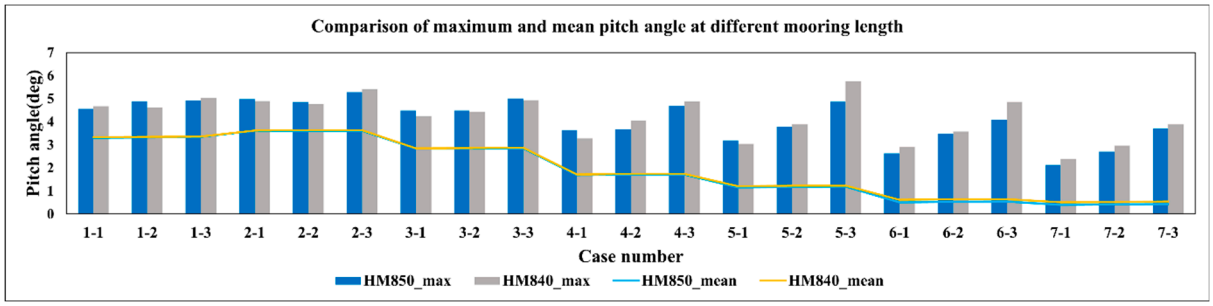


Figure 21. Comparison of the maximum and mean value of pitch angle at different mooring positions.

4.3. The Mooring Failure Scenario

As a final step, scenarios of failure by the mooring in which the mooring lines were equipped with a redundancy system were considered. Two main failure scenarios were selected, both under conditions of head waves. The first was the failure of Mooring Line 1. The other was the failure of Mooring Line 3. It was expected that the movement of the equilibrium state of the floater when a mooring line fails would be as shown in Figure 24. For the same DLCs considered in the previous section, we confirmed the details of the changes in the horizontal movement and mooring tension.

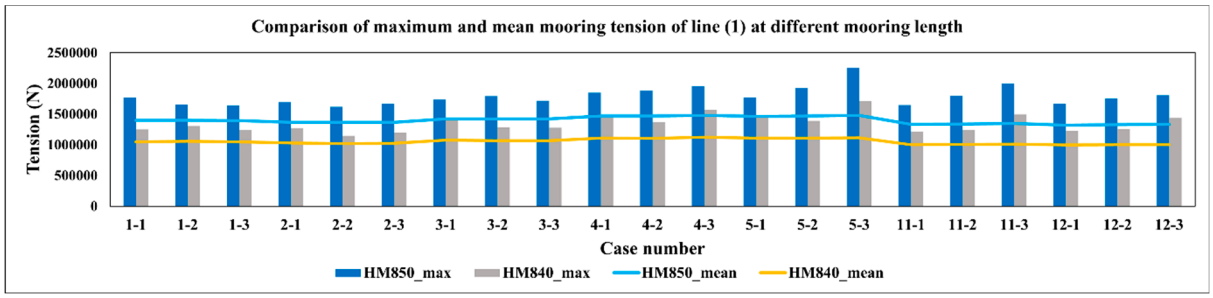


Figure 22. Comparison of the maximum and mean value of mooring tension for Line 1 at different mooring positions.

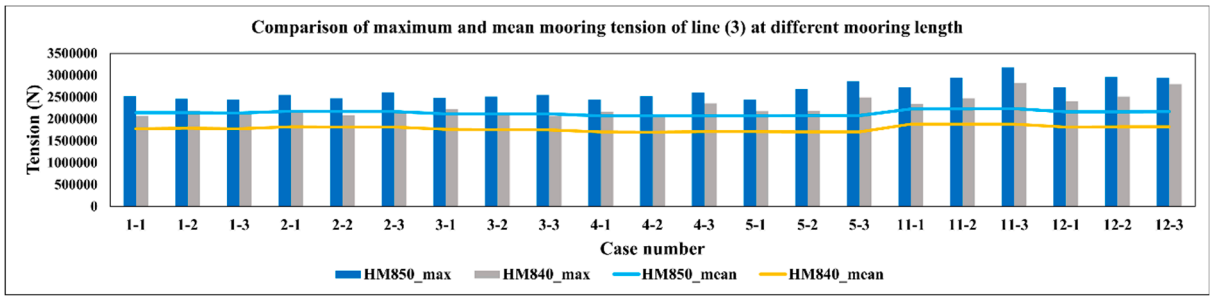


Figure 23. Comparison of the maximum and mean value of mooring tension for Line 3 at different mooring positions.

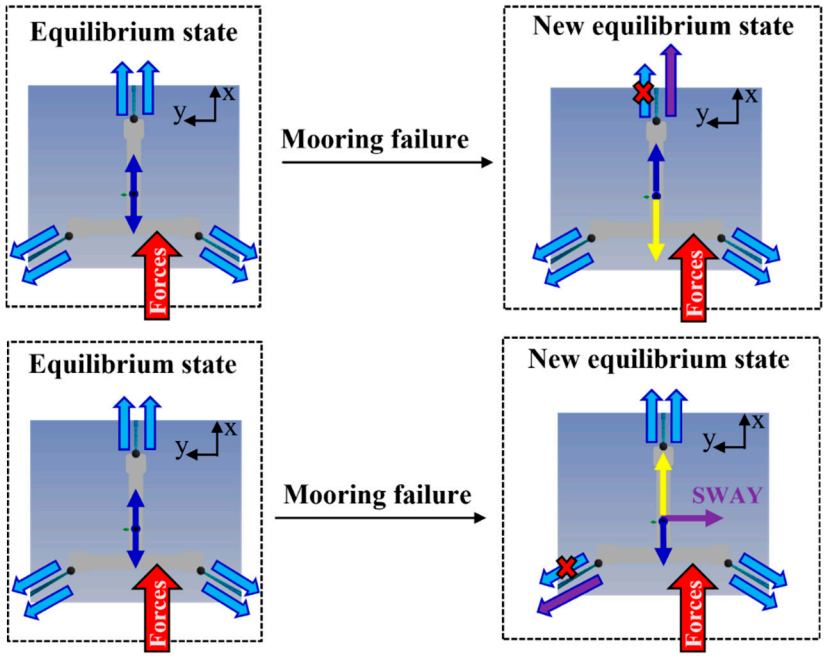


Figure 24. Movement of the equilibrium state due to failure of the mooring.

Figures 25 and 26 show the horizontal movement and pitch angle for Case 6.1 (DLC 6.1) when Mooring Line 1 failed. When the mooring line failed, the position of the floater moved to a safe enough region, and the mean pitch angle became smaller. Sway motion also appeared, but its value was very small, as shown in Figure 27. Although one mooring line failed, the other mooring line prepared in the redundancy system kept the floater safe. Due to the movement of the floater's equilibrium position, the mooring line's tension also had different values. Figure 28 shows the time series of mooring tension of Lines 2, 4, and

5. When Mooring Line 1 failed, Mooring Line 2, which provided redundancy for Line 1, had high mooring tension, but the other mooring lines had a small amount of tension due to the movement of the equilibrium position.

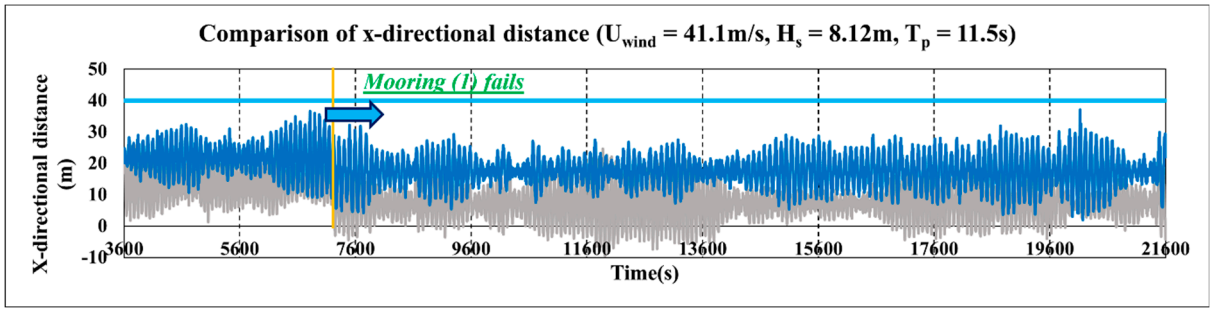


Figure 25. Change in the horizontal movement for the failure of Mooring Line 1 (Case 6-1; blue, 840 m; gray, 850 m).

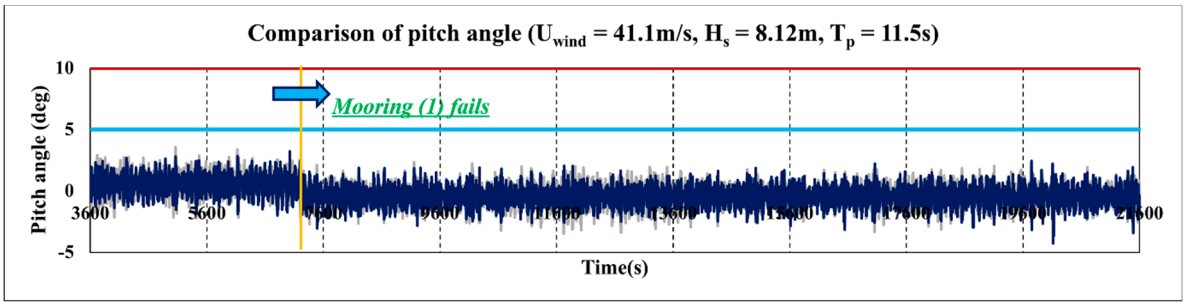


Figure 26. Change in the pitch angle for the failure of Mooring Line 1 (Case 6-1).

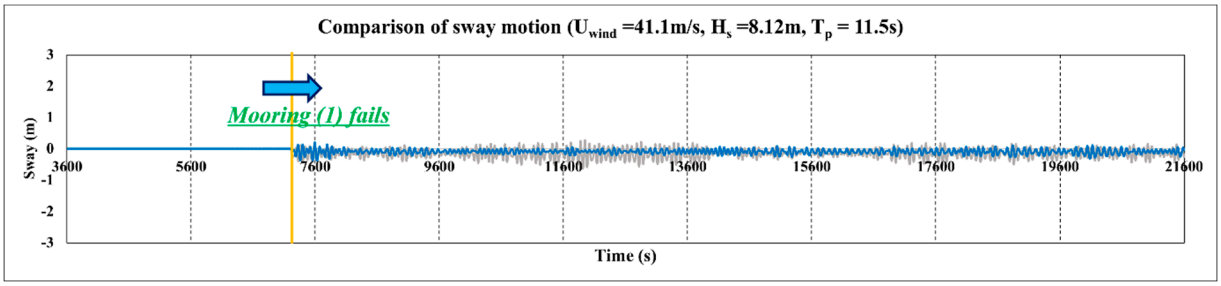


Figure 27. Change in the sway motion for the failure of Mooring Line 1 (Case 6-1; blue, 840 m; gray, 830 m).

Next, the responses when Mooring Line 3 failed under head wave conditions were studied. Figures 29 and 30 show the changes in the movement in the x direction and the pitch angle of the floater when Mooring Line 3 became disconnected from the floater. Unlike its behavior after the failure of Line 1, the floater moved far from the original positions, and the movement became more than 40 m when the horizontal mooring length was 840 m. The overall pitch angle also increased after the failure. The equilibrium position in the y direction changed, and Figure 31 shows that a large sway motion appeared when the mooring line failed. Finally, as can be seen in Figure 32, which displays the mooring tension of each line, Mooring Line 4 experienced high tension, and the other mooring lines' tension decreased. However, the increase in the tension of the redundant mooring lines was very large compared with the case of the failure of Mooring Line 1. In Figure 33, which show the root mean square (RMS) of the mooring tension of each line, it can be seen that the failure of Mooring Line 3 increased the tension in the redundant lines. Thus, it seems that the failure of Line 3 was more critical for the floater and the mooring system. Finally, the root

mean square of the mooring tension of each line at the fairlead point (i.e., Lines 2, 4, and 5) is shown in Figure 33. The failure of Line 1 makes Line 2 experience higher tension than normal, but the increase after failure is very great for Line 4 when Mooring Line 3 fails at both horizontal mooring lengths.

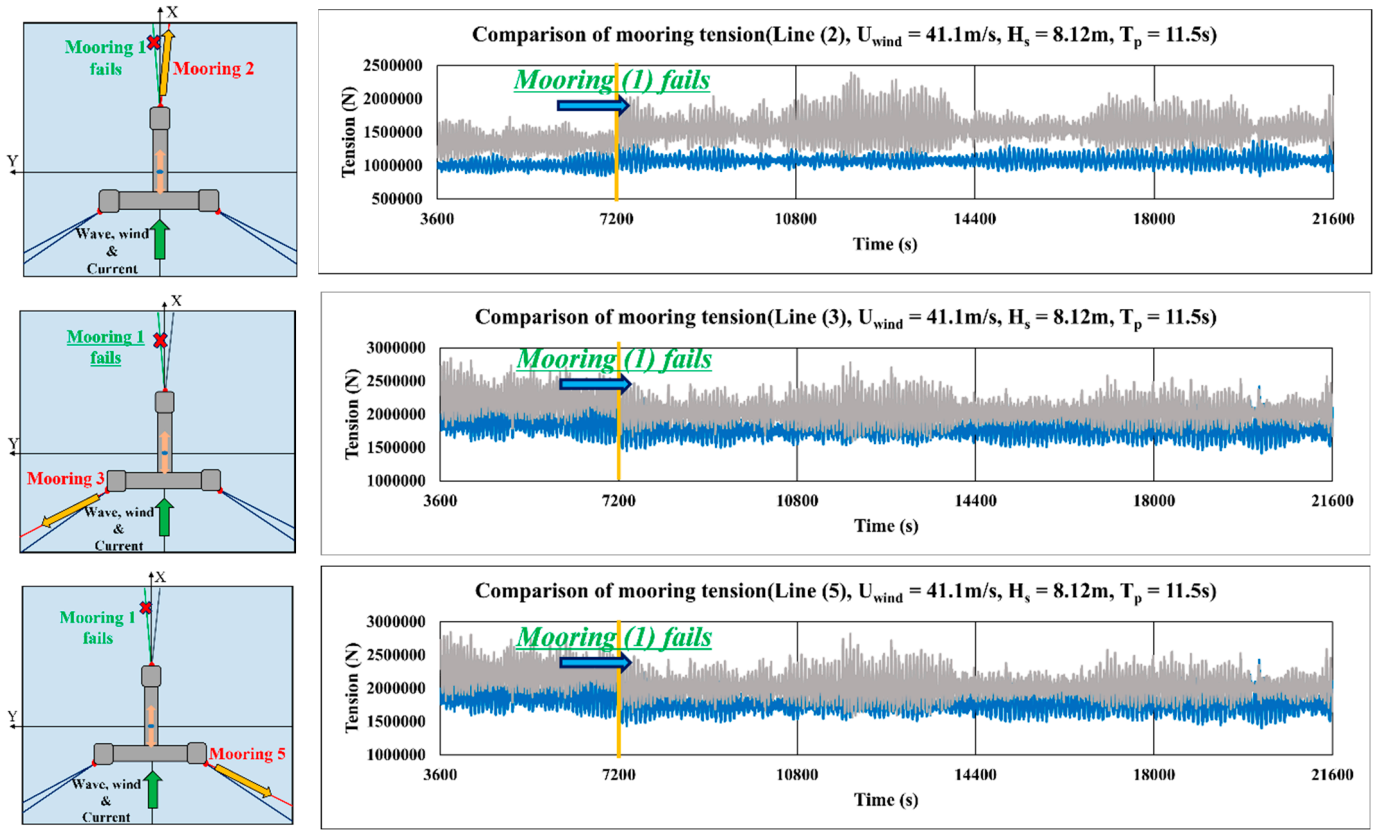


Figure 28. Change in the mooring tension of Lines 2, 3, and 5 for the failure of Mooring Line 1 (Case 6-1; blue, 840 m; gray, 850 m; Yellow arrows mean direction of tension, Green arrow means direction of environmental loads).

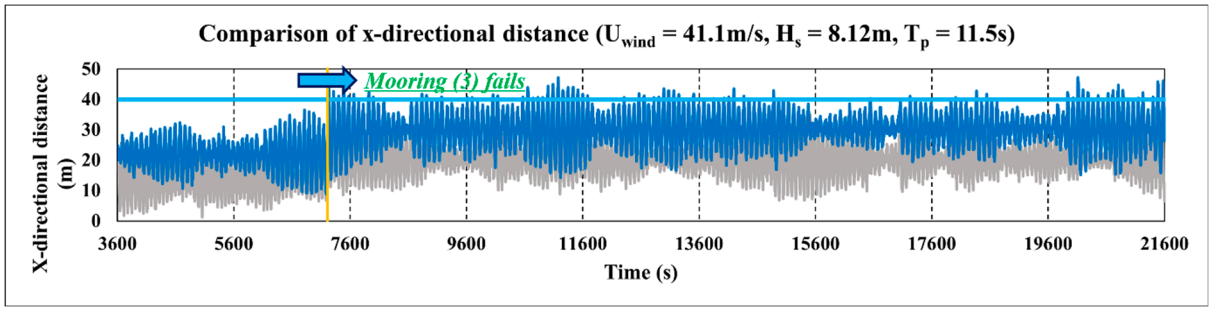


Figure 29. Change in horizontal movement for the failure of Mooring Line 3 (Case 6-1; blue, 840 m; gray, 850 m).

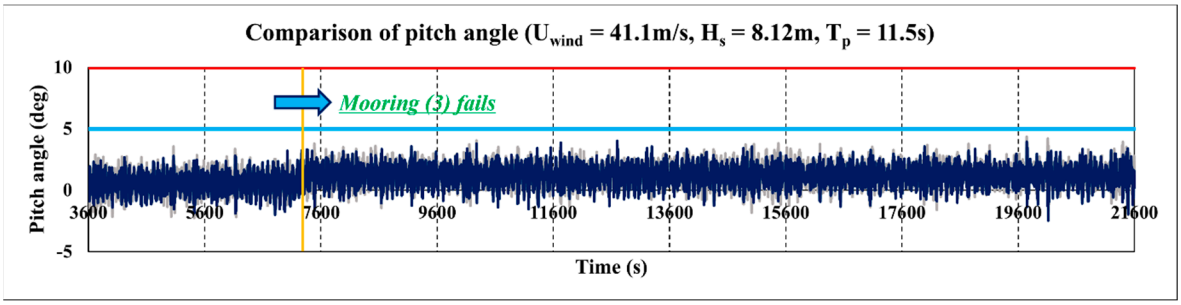


Figure 30. Change in the pitch angle for the failure of Mooring Line 3 (Case 6-1).

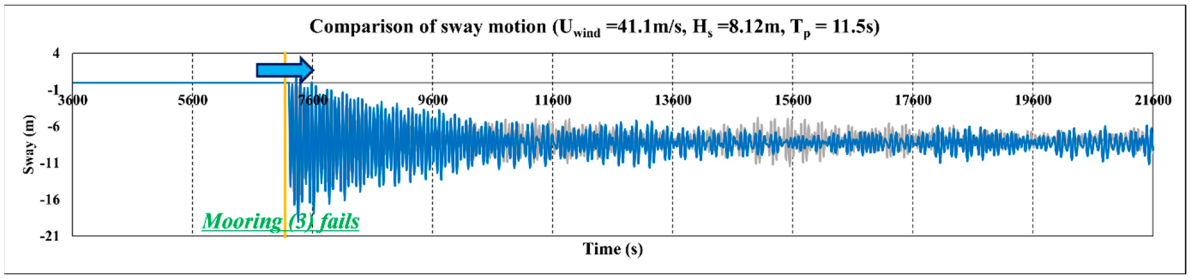


Figure 31. Change in the sway motion for the failure of Mooring Line 3 (Case 6-1; blue, 840 m; gray, 850 m).

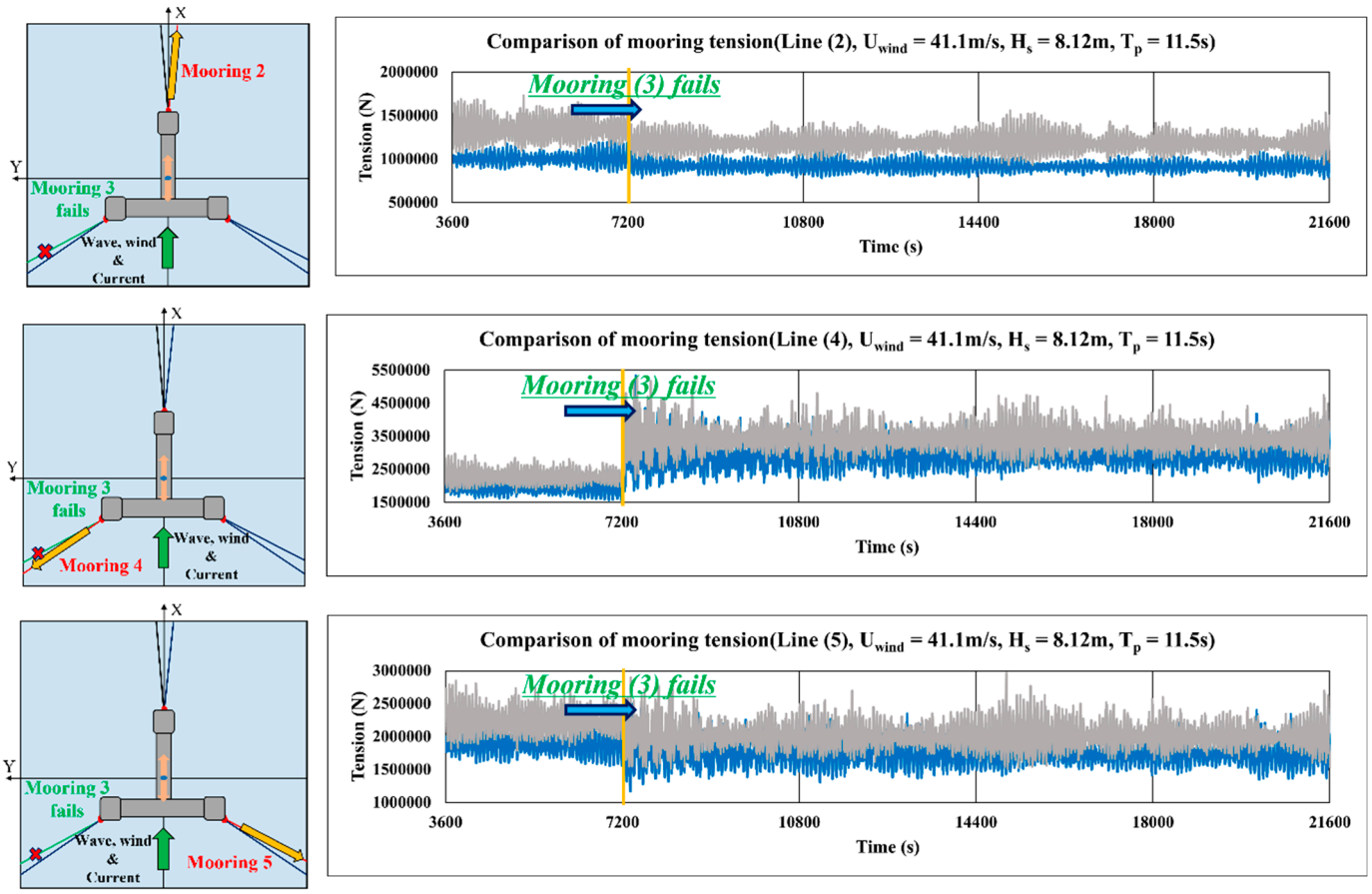


Figure 32. Change in the mooring tension of Lines 2, 4, and 5 for the failure of Mooring Line 3 (Case 6-1; blue, 840 m; gray, 850 m; Yellow arrows mean direction of tension, Green arrow means direction of environmental loads).

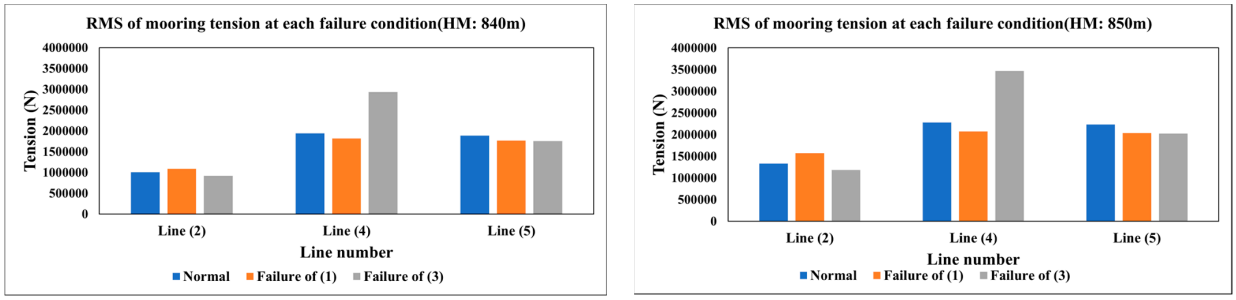


Figure 33. Root mean square of mooring tension at each horizontal mooring length in Case 6.1. Left: 840 m; right: 850 m.

5. Conclusions

The motion responses of a floating substructure (the Tri-Star floater with a 9.5 MW VESTAS wind turbine) were numerically studied using time-domain simulation. Considering the numerous environmental conditions recommended in DLC 1.6 and 6.1 of IEC 61400-3-1, several motion criteria were checked. After several parametric studies, two different touchdown positions in the same mooring length were selected, and the effect of the suspended length on the motion response was also confirmed. The results showed that the horizontal movement of the floater was strongly influenced by the suspended mooring length, and a short, suspended line had relatively little tension and a large horizontal motion. On the other hand, the pitch angle was generally not influenced by the mooring line's position because of the existence of the hydrostatic restoring force. From the 36 case studies, it is confirmed that tilt angle is more critical at DLC 1.6, and horizontal distance is generally large at DLC 6.1. In a mooring system with redundancy at each fairlead point, scenarios of mooring failures were considered in a time-domain simulation. The responses were obtained after the mooring failed. Although the results are not shown here, a mooring system without redundancy had a very large amount of drift, and it did not satisfy the criteria. On the other hand, the mooring with a redundancy system gave the floater a safe enough motion response after one mooring line failed. The floater obtained a new equilibrium, and additional motion appeared. It was also confirmed that the failure of the mooring line located in the crossflow direction (Mooring lines 3, 4, 5, and 6) was more critical than that of the mooring line located in the direction of the waves (Mooring lines 1 and 2) for both the motion response and the mooring tension under head wave conditions.

Author Contributions: Conceptualization, K.H., R.-H.Y. and D.L.; Methodology, K.H. and D.L.; Software, H.P.; Validation, K.H. and R.-H.Y.; Formal analysis, K.H. and H.P.; Investigation, H.P.; Writing—Original draft, K.H.; Writing—Review & editing, R.-H.Y. and D.L.; Supervision, D.L. All authors have read and agreed to the published version of the manuscript.

Funding: This work was supported by the Human Resources Development of the Korea Institute of Energy Technology Evaluation and Planning (KETEP) grant funded by the Korean government (Ministry of Trade, Industry and Energy) (No. 20214000000180) and by the Korea Institute of Energy Technology Evaluation and Planning (KETEP) grant funded by the Korean government (MOTIE) (20224000000220, Jeonbuk Regional Energy Cluster Training of human resources).

Data Availability Statement: Data are contained within the article.

Conflicts of Interest: Author Rae-Hyoung Yuck was employed by the Samsung Heavy Industry. The remaining authors declare that the research was conducted in the absence of any commercial or financial relationships that could be construed as a potential conflict of interest.

References

1. Hao, E.; Liu, C. Evaluation and comparison of anti-impact performance to offshore wind turbine foundations: Monopile, tripod, and jacket. *Ocean Eng.* **2017**, *130*, 218–227. [CrossRef]

2. Beyer, F.; Choisnet, T.; Kretschmer, M.; Cheng, P.W. Coupled MBS-CFD simulation of the IDEOL floating offshore wind turbine foundation compared to wave tank model test data. In Proceedings of the Twenty-fifth International Ocean and Polar Engineering Conference, Kona, HI, USA, 21–26 June 2015; OnePetro: Richardson, TX, USA, 2015.
3. Márquez, L.; Le Sourne, H.; Rigo, P. Mechanical model for the analysis of ship collisions against reinforced concrete floaters of offshore wind turbines. *Ocean Eng.* **2022**, *261*, 111987. [CrossRef]
4. Liu, Y.; Li, S.; Yi, Q.; Chen, D. Developments in semi-submersible floating foundations supporting wind turbines: A comprehensive review. *Renew. Sustain. Energy Rev.* **2016**, *60*, 433–449. [CrossRef]
5. Yang, Y.; Bashir, M.; Michailides, C.; Li, C.; Wang, J. Development and application of an aero-hydro-servo-elastic coupling framework for analysis of floating offshore wind turbines. *Renew. Energy* **2020**, *161*, 606–625. [CrossRef]
6. Chen, J.; Hu, Z.; Liu, G.; Wan, D. Coupled aero-hydro-servo-elastic methods for floating wind turbines. *Renew. Energy* **2019**, *130*, 139–153. [CrossRef]
7. Niranjan, R.; Ramisetti, S.B. Insights from detailed numerical investigation of 15 MW offshore semi-submersible wind turbine using aero-hydro-servo-elastic code. *Ocean Eng.* **2022**, *251*, 111024. [CrossRef]
8. Otter, A.; Murphy, J.; Pakrashi, V.; Robertson, A.; Desmond, C. A review of modelling techniques for floating offshore wind turbines. *Wind Energy* **2022**, *25*, 831–857. [CrossRef]
9. Jonkman, J.M.; Buhl, M.L. *FAST User's Guide*; National Renewable Energy Laboratory: Golden, CO, USA, 2005; Volume 365, p. 366.
10. Jonkman, J.; Butterfield, S.; Musial, W.; Scott, G. *Definition of a 5-MW Reference Wind Turbine for Offshore System Development*; (No. NREL/TP-500-38060); National Renewable Energy Laboratory (NREL): Golden, CO, USA, 2009.
11. Bak, C.; Zahle, F.; Bitsche, R.; Kim, T.; Yde, A.; Henriksen, L.C.; Natarajan, A. The DTU 10-MW reference wind turbine. In *Danish Wind Power Research*; 2800; DTU Wind Energy: Kongens Lyngby, Denmark, 2013.
12. Pegalajar-Jurado, A.; Bredmose, H.; Borg, M.; Straume, J.G.; Landbø, T.; Andersen, H.S.; Lemmer, F. State-of-the-art model for the LIFES50+ OO-Star Wind Floater Semi 10MW floating wind turbine. In *Journal of Physics: Conference Series*; IOP Publishing: Philadelphia, PA, USA, 2018; Volume 1104, p. 012024.
13. Gaertner, E.; Rinker, J.; Sethuraman, L.; Zahle, F.; Anderson, B.; Barter, G.E.; Viselli, A. *IEA Wind TCP Task 37: Definition of the IEA 15-Megawatt Offshore Reference Wind Turbine*; (No. NREL/TP-5000-75698); National Renewable Energy Laboratory (NREL): Golden, CO, USA, 2020.
14. Allen, C.; Viscelli, A.; Dagher, H.; Goupee, A.; Gaertner, E.; Abbas, N.; Barter, G. *Definition of the UMaine VolturnUS-S Reference Platform Developed for the IEA Wind 15-Megawatt Offshore Reference Wind Turbine*; (No., NREL/TP-5000-76773); National Renewable Energy Lab. (NREL): Golden, CO, USA; University of Maine: Orono, ME, USA, 2020.
15. Zhang, L.; Shi, W.; Karimirad, M.; Michailides, C.; Jiang, Z. Second-order hydrodynamic effects on the response of three semisubmersible floating offshore wind turbines. *Ocean Eng.* **2020**, *207*, 107371. [CrossRef]
16. Shao, Y.; Zheng, Z.; Liang, H.; Chen, J. A consistent second-order hydrodynamic model in the time domain for floating structures with large horizontal motions. *Comput.-Aided Civ. Infrastruct. Eng.* **2022**, *37*, 894–914. [CrossRef]
17. Micallef, D.; Rezaeiha, A. Floating offshore wind turbine aerodynamics: Trends and future challenges. *Renew. Sustain. Energy Rev.* **2021**, *152*, 111696. [CrossRef]
18. Subbulakshmi, A.; Verma, M.; Keerthana, M.; Sasmal, S.; Harikrishna, P.; Kapuria, S. Recent advances in experimental and numerical methods for dynamic analysis of floating offshore wind turbines—An integrated review. *Renew. Sustain. Energy Rev.* **2022**, *164*, 112525. [CrossRef]
19. Barooni, M.; Ashuri, T.; Velioglu Sogut, D.; Wood, S.; Ghaderpour Taleghani, S. Floating Offshore Wind Turbines: Current Status and Future Prospects. *Energies* **2022**, *16*, 2. [CrossRef]
20. Cummins, W.E. *The Impulse Response Function and Ship Motions*; David Taylor Model Basin: Washington, DC, USA, 1962.
21. Newman, J.N. Second-order slowly varying forces on vessels in irregular waves. In Proceedings of the International Symposium on Dynamics of Marine Vehicles and Structures in Waves, London, UK, 1–5 April 1974.
22. Hasselmann, K.; Barnett, T.P.; Bouws, E.; Carlson, H.; Cartwright, D.E.; Enke, K.; Walden, H. *Measurements of Wind-Wave Growth and Swell Decay during the Joint North Sea Wave Project (JONSWAP)*; German Hydrographic Institute: Hamburg, Germany, 1973.
23. Choi, Y.H.; Kim, H.J.; Lee, Y.J.; Yuck, R.H. Conversion of Wind and Waves with Reference Periods for the Donghae Gas Field. *Int. J. Offshore Polar Eng.* **2022**, *32*, 97–106. [CrossRef]
24. Choi, Y.-R. Analytic investigation of multi-component elastic cables under 3-D concentrated static loads. *J. Ocean Eng. Technol.* **2014**, *28*, 193–198. (In Korean) [CrossRef]
25. Choi, Y.H.; Kim, H.J. Environmental Conditions of Donghae Gas Field for FOWT. *J. Wind. Energy* **2021**, *12*, 32–44. (In Korean)
26. Tran, T.T.; Kim, E.; Lee, D. Development of a 3-legged jacket substructure for installation in the southwest offshore wind farm in South Korea. *Ocean Eng.* **2022**, *246*, 110643. [CrossRef]
27. *DNV-ST-0126*; Support Structures for Wind Turbines. Det Norske Veritas: Hovik, Norway, 2021.

Disclaimer/Publisher's Note: The statements, opinions and data contained in all publications are solely those of the individual author(s) and contributor(s) and not of MDPI and/or the editor(s). MDPI and/or the editor(s) disclaim responsibility for any injury to people or property resulting from any ideas, methods, instructions or products referred to in the content.